UNIVERSITÀ DEGLI STUDI DI PALERMO
Dottorato di Ricerca in Medicina Molecolare e Biotecnologie
Dipartimento di Biopatologia e Biotecnologie Mediche (DIBIMED)
Settore Scientifico Disciplinare MED/36

Multiparametric-MRI evaluation of cervical nodes in patients with head and neck squamous cell carcinoma (HNSCC)

IL DOTTORE
Chiara Tudisca

IL COORDINATORE
Prof. Calogero Caruso

IL TUTOR
Prof. Massimo Midiri

CICLO XXIX
ANNO CONSEGUIMENTO TITOLO 2017

INDEX

I. INTRODUCTION

In evaluating the head and neck (H&N) malignancy, as well as in other anatomical areas, the earliest and detailed identification of metastatic lymph node drainage station is decisive for the staging of the disease, and at the mean time the staging influences decisively the therapeutic approach and patient outcome, changing the strategies of combined therapies (surgery, chemotherapy and radiotherapy).

Indeed, disease recurrence following therapy occurs in 50% of patients with head and neck squamous cell carcinoma (HNSCC) who present nodal metastases at initial staging [1]. Prognosis is adversely affected by increasing number of involved nodes, nodes at lower anatomical levels, and microscopic or macroscopic extra-nodal disease extension [2-10]. An accurate staging of nodal disease is pivotal for therapy selection and subsequent surveillance.

The morphological Magnetic Resonance (MR) criteria have been, and continue to be, a strong point in the imaging evaluation of latero-cervical nodes metastases, with particular emphasis to the distinction between benign and malignant disease; although these morphological criteria are, as said, of capital importance in the evaluation of lymphadenopathy, should be noted, however, the not infrequent occurrence of a late or missed detection of metastatic lymph node localization of neoplastic disease especially, obviously, for metastatic lymph nodes of small size.

The MR morphological imaging integration with functional MR imaging (fMRI) studies such as the study of diffusion (Diffusion Weighted Imaging - DWI) but also with the assessment of perfusion (Dynamic Contrast Enhanced - DCE) and tissue oxygen consumption (blood-oxygen-level dependent - BOLD), enriches the spectrum of MR semiotics, increasing and standardizing diagnostic confidence in the identification and characterization of disease.

The use of MR-DWI in the evaluation of H&N area is to date widely documented in the literature and it have to be used in the routine MR practice for both characterization of the lesions and staging of the disease. In particular, numerous studies report that ADC values, with increasing

confidence, allow the identification and characterization of disease in the head and neck [11]. But, to our knowledge, no one investigated the other new techniques (above mentioned) that are today available to extract additional functional parameters from diffusion-weighted images (in particular the two different components, one of perfusion (ADCfast) and the other of diffusion (ADCslow), which contributes to production of the imaging signal in diffusion), which maybe would be more robust than standard ADC quantitation, as well as the oxygenation parameters on BOLD images and pharmacokinetic (PK) parameters in DCE-MR.

II. PURPOSE OF THE STUDY

To assess multiparametric-MR characteristics of nodes in patients with HNSCC to distinguish between normal and metastatic node, to allow the clinicians to start an adequate therapy according to nodes characteristics.

We studied new functional MR parameters to demonstrate their usefulness and greater diagnostic value in differentiate different types of nodes, in particular evaluating the DWI imaging to assess multi-scale (median region of interest values, inter-voxel histogram distributions, and intravoxel diffusion heterogeneity) apparent diffusion coefficient (ADC) parameters as classifiers of nodal status. Moreover we explored T2* changes in cancerous lymph nodes between breathing room air and 100% oxygen, comparing our population with a group of healthy volunteers, and finally we calculate quantitative PK parameters in DCE-MR.

III. MATERIALS AND METHODS

III.1. Patients selection

Twenty-four consecutive patients (17 male [mean age, 58.6 years; range, 43.6 to 79.5 years], 7 female [mean age, 61.1 years; range, 52.7 to 74.9 years]) satisfying inclusion criteria of histologically confirmed HNSCC with cervical nodal (N2a/N2b/N2c/N3) metastatic disease were recruited prior to primary chemo-radiotherapy. Moreover we evaluated 10 healthy volunteers [mean age 47.7 years; range, 19.7 to 75.0 years] with no previous history or current clinical/radiological suspicion of cancer, recruited from a pool of patients undergoing neck MRI for mechanical causes of neck pain.

Exclusion criteria were those relating to MR (i.e. claustrophobia, pacemaker, metallic implant, severe claustrophobia). There were no other exclusions.

All selected patients were at their first diagnosis, not receiving therapy at the time of H&N MR scan/study, and underwent over the MR study, contrast enhanced neck computed tomography (CECT) and ultrasound evaluation of the neck ± fine needle aspiration (FNA), as part of routine clinical practice for the pre-treatment staging of the disease prior to chemotherapy and radiation therapy or surgery; all the patients gave informed consent for additional MR DWI, DCE and BOLD imaging. Moreover all MR scans were performed before the execution of eventual FNA by ultrasound (done to classify all equivocal nodes).

III.2. MR study protocol

All the MR examination were performed on a 1.5T Siemens Avanto (Siemens, Erlangen, Germany) magnet, using the manufacturer's carotid coils.

Table 1 summarizes the characteristics of the sequences that we used.

Axial T2 weighted Periodically Rotated Overlapping ParallEL Lines with Enhanced Reconstruction (PROPELLER) images (figure 1) of the neck (base of skull to upper thorax) were acquired supine. Axial DWI of the same area were acquired with a Short Tau Inversion Recovery - Echo Planar Imaging (STIR-EPI) sequence using diffusion gradients applied in 3 orthogonal directions at each of 6 b-values (0, 50, 100, 300, 600 and 1000s/mm2) (figure 2).

For BOLD imaging a T2* weighted imaging was performed on the axial plane, initially whilst breathing room air, using a conventional multiple-echo gradient echo sequence (echo times 12, 24, 36 and 48 ms) to acquire four axial sets of images (figure 3). For each participant T2* weighted imaging was repeated within the same session after inhalation of 100% oxygen at 15L/min for four minutes via a face mask, with continued delivery of oxygen during the scan.

DCE-MRI was performed on a coronal view with a T1 weighted volumetric FLASH sequence with TR/TE 2.3/1.0 ms, flip angle 10^{o}, field of view 269 mm, slice thickness 4 mm, temporal resolution of 3 seconds, and number of time points 50.

For DWI images, trace diffusion-weighted images for each slice were automatically reconstructed using the manufacturers workstation (Siemens, Erlangen, Germany). ADC maps (figure 4) using all 6 b-values (ADC_{6b}), low b-values alone (0, 50 and 100) (ADC_{fast}), and high b-values alone (300, 600 and 1000) (ADC_{slow}) were derived from the trace images by a mono-exponential non-linear least squares (Levenberg-Marquardt algorithm) fit performed using a commercial software package (MATLAB 2011b, The MathWorks Inc., Natick, MA, 2000). A further stretched exponential fit was performed using the same software and α value and stretched exponential distributed diffusion coefficient (DDC) maps derived (figure 4). The stretched exponential model was described by:

$$S(b)/S_0 = \exp(-(b \times DDC)^{\alpha})$$

Where S(b) was the signal intensity with a diffusion weighting of b, S_0 is the signal on the b0 image, b is the b-value, and the index α relates to the diffusion heterogeneity within the voxel (ranging from 0 to 1), DDC is the distributed diffusion coefficient and represents the mean intravoxel diffusion rates. A α value of 1 indicates mono-exponential diffusion, whilst that nearer to 0 multi-exponential diffusion [12].

T2* maps (on room air and 100% oxygen) were derived by performing fits of a standard exponential relaxation model (S = Ke–TE/T2*) to the data on a pixel-by-pixel basis, using a commercial software package (MATLAB 2011b, The MathWorks Inc., Natick, MA, 2000) (figure 5).

In the DCE images, for each node a single slice of the DCE was selected, where the node was better seen on his major/maximum dimension, and a manually region of interest (ROI) was drawn at the level of the external capsule, excluding the colliquate region from the inclusion in the ROI.

PK parameters were derivered for each node, using both the simplex and the Bayesian inference algorithm.

III.3. Nodal staging

Two experienced H&N radiologists (with 7 years and 15 years of H&N experience, respectively) reviewed all CECT and MR and performed ultrasound evaluation of the neck in all patients.

Cervical nodes were assessed as per the UICC:TNM Classification of Malignant Tumours [13]. N2a/N2b (single > 3cm but ≤ 6cm greatest axis, or metastases in multiple ipsilateral nodes < 6cm), N2c (bilateral or contralateral lymph nodes, none more than 6 cm in greatest dimension) or N3 (nodes > 6cm in short axis) status was done.

All equivocal imaging features (>0.6 cm short axis, round contour, irregular margins, necrosis, heterogeneous enhancement on CT/MR) were sampled at the time of ultrasound by fine needle

aspiration (FNA) and classified by in-room cytology. The location of all sampled nodes was marked on the anatomical MR for subsequent quantitative analysis on functional images. Consenting patients with confirmed cervical N2a/N2b/N2c or N3 disease were recruited.

III.4. Image analyses

Image analysis were conducting using Jim 5.0 software (Xinapse Systems, Thorpe, Waterville, UK) for DWI and BOLD maps, and using OsiriX platform for morphological sequence visualization and DCE enhancement curve evaluation and DCE enhancement curve values extraction. Two radiologists in consensus (BLINDED FOR REVIEW), aware of the location of sampled nodes and nodal status at conventional staging but unaware of the ADC maps, reviewed the PROPELLER and trace weighted diffusion images. Trace DWI for each slice were automatically reconstructed using the manufacturers workstation (Siemens, Erlangen, Germany).

They contoured a ROI on b300 images on each imaging slice containing the metastatic node, encompassing all solid nodal tissue while avoiding any macroscopic necrotic areas (focal areas of high signal on T2 weighted PROPELLER images – figure 1). They also evaluated the images of the healthy volunteers to identify normal/reactive nodes, and even in this case they drawn an ROI on b300 images to encompass the node. Overall at least one metastatic or one benign node was contoured for each patient and volunteer respectively.

The ROIs from the b300 images were transferred electronically to corresponding ADC parameter maps (ADC6b, ADCfast and ADCslow, α value and DDC), and a list of voxel by voxel parameter values for metastatic and benign cervical nodes derived. Median values for the entire tissue volume for benign and metastatic nodes were calculated for each parametric map.

The same radiologists confirmed and contoured the location of metastatic lymph nodes in patients and normal nodes in healthy volunteers, on 24 ms T2* weighted images with reference to the anatomical T2-weighted MRI sequence.

For each node the entire volume of the node was contoured excluded only cystic areas of necrosis. Contours were automatically transferred from the 24 ms T2* image to air and 100% T2* maps for extraction of quantitative pixel based histographic T2* data. The median, skewness and kurtosis of pixel histograms were derived for each node from the T2* map on air and also the T2* map on 100% oxygen. Quantitative histographic parameters derived from room air T2* maps and from 100% oxygen T2* maps were compared between normal and metastatic nodes. Change in the histographic parameter between the breathing room air and 100% oxygen was calculated for metastatic and normal lymph nodes.

Finally, for each node a single slice of the DCE was selected, where the node was better seen on his major/maximum dimension, and a manually ROI was drawn at the level of the external capsule, also in this case avoiding any colliquate/necrotic area.

DCE enhancement curve values were extracted, and then was done a quantification of pharmacokinetic (PK) parameters using simplex and Bayesian inference algorithms.

The PK parameters were initialized as vp0= 0.05, Ktrans0= 0.4 min-1, ve0= 0.5. Onset time was initialized with the time point the contrast agent was administered.

The simplex and Bayesian inference algorithms were run using multiple initializations of the PK parameters. Specifically 15 different initializations were generated using uniform distributions supported within intervals as described by the following formulas: vp0= unif (0, 0.2), Ktrans0= unif (0.1, 1.0), ve0= unif (0.3, 0.6).

The population distribution histogram of each parameter for benign and metastatic nodal volumes was plotted and skewness of the distributions recorded.

III.5. Statistical analysis

All statistical analysis were conducting using a commercial statistic package (Prism 6.0 for Mac, GraphPad Software, San Diego California USA).

Normality of data was assessed using the D'Agostino and Pearson omnibus normality test.

III.5.a. Benign verses metastatic comparison

Histogram skewness and median values of ADC6b, ADCfast and ADCslow, α value and DDC, were compared between benign and metastatic cervical nodes using the Mann Whitney test, as well as for the mean of T2* histogram median, skewness and kurtosis values in room air and 100% oxygen breath.

A Mann–Whitney U test (MWU sig) was performed to compare the median values of the PK DCE parameters between normal and cancer ROIs.

III.5.b. ADC parameter comparison

Differences between median ADC6b, ADCfast, ADCslow and DDC for parameters for individual patients were assessed using Friedman statistics with a Dunn's post-test.

III.5.c. DCE parameters evaluation

Separate univariate logistic regression models were built for the PK parameters derived using the simplex and the Bayesian inference algorithm. The ability of individual pharmacokinetic parameters to predict cancer was assessed by receiver operator characteristic (ROC) area under curve (AUC) analysis.

Leave-one-out analysis [14] was used to assess the accuracy of predictive models on independent samples. One case (out of the total patient population) was excluded, and a model generated from the remainder of the cases. The model was then tested on the excluded case and a predictive

probability calculated. The process was repeated for all cases, excluding successive cases in turn allowing calculation of a predictive probability per case. A ROC (LOO ROC) was then created using the derived predictive probabilities.

ROC curves were compared using the significance test suggested by Hanley and McNeil [20].

IV. RESULTS

Patient demographics, primary tumor site and TNM stage are shown in table 2.

The radiologists identified 84 metastatic nodes on the 24 patients, and 40 normal nodes on the 10 healthy volunteers.

IV.1. DWI analysis

D'Agostino and Pearson omnibus normality test results for parametric values across patients are shown in table 3 and 4.

IV.1.a. Benign verses metastatic comparison

IV.1.a.I. Single volumetric ROI analysis

Median parametric values for benign and malignant nodes are given in table 3. Median ADC_{fast} was lower in metastatic (1.56 x $10^{-3}mm^2/s$) than benign (1.76 x $10^{-3}mm^2/s$) nodes (p=0.0458). There was no significant difference between benign and metastatic nodes for all other parameters (p=0.0513 to 0.1575). Intra-voxel ADC heterogeneity was greater in benign verses metastatic nodes (α value:0.73 and 0.77; p=0.026).

IV.1.a.II. Histogram voxel population distribution analysis

Median skewness values across patients for individual parameters for benign and metastatic nodes are given in table 4. Inter-voxel histogram distributions of ADC_{6b} (1.65 vs. 1.15; p=0.0028), ADC_{slow} (0,984 vs. 0.394 ; p<0.0001) and DDC (1.573 vs. 1.046; p=0.0055) were more positively skewed in metastatic nodes.

There was no significant difference for histogram skewness between benign and metastatic nodes for the remain derived parameter (ADC_{fast} p=0.095 and α p=0.1167).

IV.1.b. ADC parameter comparison - Difference analysis (Friedman test)

There was a significant difference between ADC_{fast} and other ADC parameters (ADC_{6b}, ADC_{slow} and DDC) and between ADC_{6b} and DDC, ADC_{slow} and DDC for metastatic nodes (Friedman and Dunn's post-test $p<0.0001$). ADC_{6b} and ADC_{slow} were not significantly different for benign nodes (Dunn's post-test $p>0.05$).

There was a significant difference between ADC_{fast} and other ADC parameters (ADC_{6b}, ADC_{slow} and DDC) and between ADC_{6b} and DDC, ADC_{slow} and DDC for metastatic nodes (Friedman and Dunn's post-test $p<0.0001$), but no significant difference between ADC_{6b} and ADC_{slow} (Dunn's post-test $p>0.05$).

IV.2. DCE analysis

IV.2.a. Comparison of PK parameters between nodal metastatic and benign ROIs

Parametric maps of a head and neck metastatic patient estimated with the simplex and the Bayesian inference algorithms are illustrated at figure 6. Fitting the estimated concentration $C(t)$ to the mean ROI concentration profile along the head and neck metastatic nodes $C_{TIC}(t)$ is also shown at figure 6. Following MWU test all the PK parameters estimated with the Bayesian inference algorithm were significantly different from the ones estimated with the simplex algorithm for both the benign and the cancer ROIs (figure 7).

IV.2.b. Univariate ROC analysis

K_{trans} was the best classifier of head and neck node metastasis for both the simplex and the Bayesian inference algorithm. According to the score test, for the simplex algorithm only K_{trans} could significantly classify metastasis, whereas for the Bayesian inference all PK parameters were significant classifiers (table 5).

Following a significance test between ROC curves the AUC (on the original population or following LOO analysis) of K_{trans} estimated with the Bayesian inference algorithm was not significantly better. Significant difference was found for the v_e AUC between the simplex and the Bayesian inference algorithm (table 5).

IV.2.c. Multiple initialisations – Robustness of evaluated algorithms

Both the simplex and the Bayesian inference algorithm were run with 15 different initializations. The interquartile range of the medians were 0.23 for the simplex algorithm and 0.01 for the Bayesian inference algorithm.

ROC-AUC were estimated per PK parameter for each initialization. Table 6 illustrates the median and interquartile range accross the 15 initializations.

IV.3. BOLD analysis

IV.3.a. Benign verses metastatic comparison

Mean histographic T2* parameters for metastatic and normal nodes are presented in table 7.

T2* median values of nodal histograms on 100% oxygen compared with room air were significantly lower for metastatic nodes ($p<0.001$) but not significantly different for normal nodes ($p=0.148$). There was a significant difference between normal and metastatic T2* median values of nodal histograms on 100% oxygen (Mann-Whitney $p=0.012$); but not on room air (Mann-Whitney $p=0.549$).

T2* nodal histograms became significantly more positively skewed ($p=0.002$) and more peaked with significantly increased kurtosis ($p=0.005$) on 100% oxygen compared with room air (figure 8).

There was no significant change in skewness or kurtosis of normal nodes between room air and 100% oxygen. There was no significant difference in skewness or kurtosis on room air or on 100% oxygen between metastatic and normal nodes (Mann-Whitney p=0.207 to 0.744).

V. DISCUSSION

V.1. Head and neck squamous cell carcinoma (HNSCC)

H&N cancer is a relative rare tumor, indeed it is one type of cancer that has increased by 7% in the last 15 years making it an increased social and economic burden.

Overall, head and neck cancer accounts for more than 500,000 cases annually worldwide [16-18].

Males are affected significantly more than females with a ratio ranging from 2:1 to 4:1.

The incidence among the population of H&N cancer is 11.2 per 100,000 people.

The primary risk factors associated with head and neck cancer include tobacco use, alcohol consumption, human papillomavirus infection (for oropharyngeal cancer), and Epstein-Barr virus infection (for nasopharyngeal cancer). The chronic exposure of the upper aerodigestive tract to these carcinogenic factors can result in dysplastic or premalignant lesions in the oropharyngeal mucosa and ultimately result in head and neck cancer.

With the improvement in medical care and advances in medical technologies, half of people diagnosed with H&N cancer now survive their disease for at least ten years and death rate has fallen by 10% over the last decade.

Most H&N cancers begin in the squamous cells that form the lining of the moist surfaces inside the mouth, the nose, and the throat [19]. These squamous cell cancers are often referred to as HNSCC, and are the most common cancer in the H&N district. H&N cancers are categorized by the areas in which they begin: oral cavity, pharynx, larynx, sinuses and nasal cavity, or salivary glands.

H&N cancers often spread to the cervical lymph nodes of the neck. This spread is often the first sign of the disease at the time of diagnosis. Lymph node involvement is the most important prognostic factor regarding the survival of patients with H&N cancer [20]. Lymph nodes can be classified by level based on anatomic landmarks that can be consistently identified on cross-sectional imaging [21].

Today with many treatment options available, it is important to have an a priori method to stratify good risk and poor risk categories to improve outcome and quality of life.

Determining the extent to which a cancer has spread is mandatory in order to plan effective treatments and remove all tumour tissues. The tumour-node-metastasis (TNM) staging system was developed to achieve consensus on one globally recognised standard for classifying the extent of spread of a cancer. Generic staging for head and neck cancer is presented in Table 8.

The presence of lymph node metastases is one of the most important prognostic indicators in HNSCC. Five year survival is reduced by 50% when a single metastatic cervical lymph node is present, and drops to 25 % in the setting of a contralateral metastatic cervical lymph node [22-23].

In addition, nodal metastatic disease not only increases the risk of local recurrence but also increases the risk of distant metastases [24-25]. Indeed disease recurrence following therapy occurs in 50% of patients with HNSCC who present with nodal metastases at initial staging [1].

Accurate lymph node classification and staging is therefore a vital component of tumor imaging and previous work has been done to unify both in the clinical and radiological spheres [21, 26].

Advancements in imaging techniques such as helical CT, MRI, and high-resolution sonography [27-31] have improved the detection of metastatic cervical nodes in patients with head and neck cancer. Accordingly, several investigators have attempted to determine reliable criteria for detecting these nodes. One of these is the criterion of size. The number of lymph nodes infiltrated with malignant cells also has an impact in predicting a patient's survival outcome.

Tumor response to radiation therapy is counteracted by three important mechanisms of resistance at the cellular level: hypoxia, accelerated proliferation, and intrinsic radiation resistance [32]. Various functional and molecular imaging techniques have been shown to be useful for monitoring these microenvironment variables in HNSCCs both before and during treatment and may help identify patients with resistant tumors that then can be treated more effectively with higher radiation doses or surgery.

Hypoxia is an established indicator of poor prognosis for patients with head and neck cancers

[33]. It leads to radiation resistance in tumor cells by preventing irreversible damage to cell deoxyribonucleic acid (DNA) by free radicals induced by ionizing radiation; oxygen is needed for the production of free radicals. Cell DNA thus undergoes repair and tumor cells survive [32]. The critical partial pressure of oxygen (pO2) threshold below which solid tumors show resistance to radiation therapy is approximately 10–15 mm Hg [33]. The amount of radiation needed to achieve cell kill in hypoxic conditions is three times that needed in normoxic conditions [34].

V.2. MRI evaluation of HNSCC lymph nodes

MRI, which has excellent soft-tissue contrast resolution and multiplanar imaging capability, has been proven to be a valuable tool for detecting and defining the extent of H&N cancers and nodes invasion [11, 27, 31].

In early T stage disease MR influences the accuracy of staging by determining whether a tumour is confined to the primary site.

Advances in H&N imaging are shifting from the morphological to the functional techniques. These techniques are being used to assess the complex interrelated processes in the cancer microenvironment, such as hypoxia, angiogenesis, pH and metabolism. These techniques have the potential to: (1) improve prediction of the cancer behaviour and response to treatment; (2) evaluate new drugs such as the antivascular agents; (3) monitor early cancer response during treatment; and (4) identify residual/recurrent cancer [11].

At present functional MRI (fMRI) is a research tool but this non-invasive versatile modality is showing great promise in head and neck cancer, in particular there are some potential applications (such as the study of diffusion (Diffusion Weighted Imaging - DWI) the assessment of tissue perfusion (Dynamic Contrast Enhanced - DCE) and tissue oxygen consumption (blood-oxygen-

level dependent – BOLD)), that in the future could be very helpful for the management of the patients, as shown from our results.

Nevertheless, fMRI is a technically challenging examination to perform on patients with H&N cancer, because acquisition is hampered by artefacts, including susceptibility artefacts and those related to movement from coughing, swallowing and breathing. Moreover, the acquisition parameters have yet to be standardized across centres, and even when similar protocols are used reproducibility can be problematic.

V.2.a. DWI-MR imaging

V.2.a.I. Physics principles of diffusion imaging

Diffusion shall mean a process of random thermal motion of the molecules, called Brownian motion, measured and expressed as diffusion coefficient. DWI-MR imaging is an imaging method that uses the diffusion of water molecules to generate contrast in MR images [35, 36]. It allows the mapping of the diffusion process of molecules, mainly water, in biological tissues, in vivo and non-invasively.

Biological tissues are composed of intra- and extra-cellular compartments. In these tissues, water molecules are in a state of continuous exchange between these two compartments.

Totally free diffusion of water molecules in biological tissues is not feasible as a result of the restriction of the diffusion of molecules that reflects interactions with many obstacles, such as macromolecules, fibers, and membranes. Diffusion in the extracellular space is restricted by macromolecules and membranous organelles, whereas di diffusion in the intracellular space is more restricted by physical (macromolecules and organelles) and chemical (specific binding and protein transitions and movements) factors and syneresis.

The measurement of diffusion in biological tissues also refers to another type of micro-movements defined as movements of perfusion [37]. The quantification of the translational movement of

diffusion of molecules in the human body, therefore, is defined as Apparent Diffusion Coefficient (ADC).

Simplifying the movement of molecules in biological tissues can be categorized into intravascular movements, intracellular or extracellular [38, 39]

The change of ADC values, the direct expression of the Brownian movement, is closely bound to the tissue microstructures. Great weight in the restriction of the diffusion of the molecules movements is attributable to the tissue composition and in particular to the cellularity and the presence of intact cell membranes.

The presence in biological tissues of hypercellular lesions (tumors), fibrosis, cytotoxic edema and abscess is due to restriction of diffusion of the molecules within the same tissue. Contrary, low cellularity tissue or presence of non-intact cell membrane allow a high movement capability to molecules [40].

DWI-MR images quantify the amount of movement of the water molecules in the tissues bringing on two-dimensional image (x, y) data derived from the measurement of the movements of water protons in the three dimensions of space (x, y, z). Diffusion imaging, developed by Stejskal and Tanner [38], it is obtained with the application on a MRI T2-weighted sequences (FSE or EPI), of a diffusion sensitizing gradients (equal and opposite) that are turned on before and after the 180-degree pulse.

DWI sequences need to be extremely fast in order to eliminate any motion within the body part - since the entire purpose of the DWI sequence is to measure infinitesimal movements of water molecules. The water molecules contained within a narrow matrix are not free to spread to "long" distances and acquire a phase dephasing during the application of the first gradient that is deleted from the power factor correction imposed by the second gradient. As a result it is not realized a loss of T2 signal intensity. The water molecules contained in a low cellularity system or with a little narrow matrix as a result of the first gradient are able to travel relatively long distances, thus

keeping the dephasing imposed by the first dephasing gradient, that will not be destroyed by the second rephrasing gradient, due to the distance covered. The result will be a loss of signal T2.

V.2.a.II. The b-value

The b-value traditionally refers to the intensity of the diffusion gradients. The b value is proportional to the amplitude of the gradient, at the time of application of the gradients and the interval elapsing between the application of a gradient and the application of the contrast gradient and is measured in seconds per square millimeter [41].

The sensitivity of diffusion sequences is modified by varying the b value and mainly by varying the amplitude [42]. At b values equal to 0 sec/mm2 free water molecules will be characterized by a normal T2 signal. At lower b values (50 → 100) correspond a signal loss of the water molecules with high mobility, as happens in the vessels. At high b values (500 → 1000) only molecules with high restriction of diffusion capacity will keep the T2 signal.

V.2.a.III. Quantitative evaluation. Apparent diffusion coefficient (ADC)

The apparent diffusion coefficient (ADC) represents the gradient of a line drawn in a Cartesian system and derived from the logarithm of relative intensity of the examined tissue signal. The calculation of the ADC needs at least data from two acquisitions with different b values. The use of a greater number of b values increases the reliability of the ADC, at the expense, however, of a substantial increase in the scanning time. The ADC value is independent of the intensity of the magnetic field and is measured for each individual pixel. The obtained ADC values are used for the construction of the related maps that reflect the tissue diffusivity differences corresponding to different values of b value [40].

V.2.a.IV. The bi-exponential decay of DWI signal. The separation of the components of perfusion and diffusion through the IVIM model.

The signal of a particular tissue decreases exponentially with increasing b-value [39, 43]. The curve which defines the decay of the diffusion signal, in fact, has a greater slope at low b values and a progressive tendency to parallelism to the x-axis to higher values of b. As consequence ADC values progressively decrease proceeding from images with lower b value towards that with higher b value.

The major component of the initial slope of the curve is the expression of a signal loss of its water molecules in rapid motion (fast-moving water molecules) that for their displacement are not rephased by the gradients applied after the 180° pulse [39, 40]. The second component of the curve, with less slope, is also an expression of the movements of its water molecules of the intra- and extracellular space (slow-moving water molecules), more sensitive to the rephasing gradient. Both components, the one given by fast-moving water molecules and the other given by slow-moving water molecules, are the expression of a movement in space, measurable and quantifiable through the DWI imaging, defined as intra-voxel inchoerent movements (IVIM).

While the "slow-moving water molecules" are subject to the randomness in the move, the "fast-moving water molecules" are oriented according to the architecture of the microcirculation it accrues, thus being, in principle, less subject to displacement randomness [44]. It should be noted, however, that the structure of the microcirculation presents spatial orientation and distribution similar to that of the random pattern and therefore is also permissible to include the "fast-moving water molecules" in the IVIM group.

The separation of the two component, of perfusion and of proper diffusion, can be obtained with the evaluation of different b values [37], as explained in the IVIM imaging model, using low b values to quantify the perfusion component and high b values for the diffusion component.

IVIM theory predicts that DWI signal will be attenuated by both tissue perfusion and diffusion [44] components, resulting in a drop of signals at the lower b-values that is more rapid than

predicted by a monoexponential (ME) model [45]. Mathematical models, such as the biexponential (BE) [44] and stretched exponential (SE) [12], have been proposed to describe this nonME behavior, and are often fitted to DWI images using nonlinear regression (NR) algorithms.

IVIM theory predicts that incoherent flow within capillaries causes dephasing of magnetization in the presence of diffusion weighting gradients [44]. Thus, diffusion-weighted image contrast reflects both capillary perfusion and diffusion of extravascular water. Water movement within these two compartments occurs at different rates; flow through capillaries (part of which will contribute to the net displacement of water in the diffusion sensitized direction) has been estimated at 0.5 mm/s [46], several orders of magnitude greater than thermal induced translational motion (1.1 x 10-3mm2/s) within the free ice water phantom used to approximate tissue diffusion [47]. However for clinical applications where b-values generally range from 0 to 1000, the loss of signal with increasing b-value approximates a bi-exponential decay [48].

Optimal ADC assessment can be performed using only two b-values for a system with isotropic mono-exponential diffusion [49]. Conversely, a minimum of 10 b-values is required for accurate bi-exponential fit [50]. Such measurements are often impractical in the clinical setting, and either compromise on anatomical volume coverage, image resolution, or significantly prolong scan times.

V.2.a.V. DWI imaging in H&N district evaluation

To date there is consensus in the literature that DWI can play a key role in the evaluation of pathology of the head and neck. Numerous studies in the literature have sanctioned the application of diffusion imaging into the routinely MRI protocols and would be good to standardize the characterization of the methodology aimed at the discrimination between benign lesions and frankly malignant lesions [51-55], based on the ADC values.

As previously said, DWI is based on IVIM, which allows visualization of molecular diffusion and microcirculation of the blood in the capillary network (perfusion) of biologic tissues. Cancer

metastasis to the regional lymph nodes may be associated with alterations in water diffusivity and microcirculation of the node. The reason why malignant tumors have lower ADC values is poorly understood. Within malignant tumors, the translational motion of water molecules is diminished due to increased extracellular space tortuosity, increased nuclear-to-cytoplasmic ratio, hyperchromatism, and hypercellularity. These histopathological characteristics of malignant tumor reduce the extracellular to intracellular volume ratio and the diffusion space available to water molecules, which reduce ADC values [51, 56]. Recent studies have derived ADC thresholds to discriminate benign from metastatic cervical nodes in head and neck SCC [55, 57-61], whereas others have been unable to demonstrate any difference [62, 63]. Methodology varies between studies, which may underpin disagreement. For example, it is recognised that ADC calculations incorporating low b-values (b<200s/mm2) are sensitive to tissue perfusion effects, whereas ADC derived from high b-values (b>200s/mm2) are unaffected [45]. Choice of b-value is thus critical. Furthermore, even when studies employ the same b-values and processing methodology, the ADC thresholds derived remain variable [57, 58-61], hampering cross-site applicability. A range of techniques is available to extract additional parameters from diffusion-weighted images which maybe more robust than standard ADC quantitation. For example, it is possible to deliberately separate perfusion and diffusion effects by acquiring a range of b-values [44]. Heterogeneity of diffusion rates within individual voxels can also be quantified by processing diffusion-weighted images using a stretched exponential model [12]. Furthermore, assessing the inter-voxel population distribution of ADC parameters within a given region has also been used to assign clinical status [64, 65].

V.2.b. BOLD imaging

BOLD technique, also called susceptibility weighted imaging (SWI), is a relatively new MR technique that provides innovative sources of contrast enhancement visualising the changes in

magnetic susceptibility that are caused by different substances like iron, haemorrhage or calcium. The basic concept of this technique is maintaining phase information into the final image, discarding phase artefacts and keeping just the local phase of interest.

Sensitivity to susceptibility effects increases, progressing from fast spin-echo (SE) to conventional SE to gradient-echo (GE) sequences, from T2-weighting to T2*-weighting, from short to long echo times and from lower to higher field strengths. Before the clinical implementation of SWI, susceptibility imaging relied only on GE sequences. SWI differs significantly from a T2*-weighted GE sequence: it is based on a long echo time (TE) high-resolution, flow- compensated, three-dimensional (3D) GE imaging technique with filtered phase information in each voxel. The combination of magnitude and phase data produces an enhanced contrast magnitude image that is particularly sensitive to haemorrhage, calcium, iron storage and slow venous blood, thus allowing a significant improvement compared with T2* GE sequences [66].

This technique, in particular, is able to distinguish paramagnetic deoxyhemoglobin (deoxyHb) from oxyhemoglobin (oxyHb - O2Hb). Appropriate T2*-weighted imaging reveals changes in vascular oxygenation. A limitation is that it is also sensitive to changes in Hb concentration, which may result from alterations in vascular volume and flow as well as interconversion of oxy- and deoxy-Hb. There- fore, this technique provides qualitative assessment of changes in oxygenation rather than quantitative measurements. This technique is widely used for functional brain mapping [67-69], where it is thought to primarily reflect changes in flow. It is starting to be applied to tumor studies.

The reason fMRI is able to detect this change is due to a fundamental difference in the paramagnetic properties of oxyHb and deoxyHb.

Deoxygenated haemoglobin is paramagnetic, increasing the MRI transverse relaxation rate (R2*) of water in blood and surronding tissues thus BOLD-MR is sensitive to pO2 within and in tissues adjacent to perfused vessels [70], whereas oxygenated haemoglobin is not, and therefore the former will cause local dephasing of protons, and thus reduce the returned signal from the tissues

in the immediate vicinity. Heavily T2* weighted sequences are used to detect this change, which is in the order of 1-5%. Thus, deoxyHb can behave like a contrast agent with long TEs for differentiating regions oxygenated from regions non oxygenated.

BOLD imaging measures inhomogeneities in the magnetic field due to changes in the level of O2 in the blood.

V.2.b.I. T2-weighted Gradient Echo Imaging*

The sequence of a multiecho gradient recalled echo (GRE) T2*-weighted imaging (T2*WI) is a relatively new MR technique. In contrast to T2 relaxation, which acquires a spin echo signal, T2* relaxation acquires a gradient echo signal. The sequence of a GRE T2*WI requires high uniformity of the magnetic field. GRE T2*WI can detect the smallest changes in uniformity in the magnetic field and can improve the detection rate of small lesions. In addition, the T2* value can indirectly reflect changes in tissue biochemical components and may be used for the early diagnosis and quantitative diagnosis of some diseases.

When placed in the static magnetic field of an MR scanner, protons in tissue (largely associated with water) will resonate with a characteristic frequency aligned to or opposed to the magnetic field. By applying external radio frequency (RF) radiation, the magnetic spins of the protons will be perturbed from the direction of the static field. When the RF pulse is removed the spins will return to their original orientation with two characteristic time constants, the spin-lattice relaxation (T1) and the spin-spin relaxation (T2).

There are further dephasing effects on T2, which is caused by the combination of two factors; the first factor is the tissue itself (in particular the molecular interactions), and the second factor is the inhomogeneity of the main magnetic field (dephasing of spins). The last factor is accounted for in the time constant T2*.

T2 relaxation of T2WI uses the 180° refocusing pulse to eliminate the inhomogeneity of the main magnetic field after turning off the RF. T2 relaxation only reflects the decay of the transverse

magnetization vector of the tissue itself. However, T2* relaxation does not use the 180° refocusing pulse to focus the pulses but uses it to switch the gradient field to generate the signal reunion after turning off the RF. fMRI uses acquisition techniques (primery multi-echo GRE sequences) that are sensitive to changes in T2*.

For the same tissue, the decay time of T2* relaxation is shorter compared to the T2 relaxation.

T2* relaxation acquires the gradient echo signal. First, it acquires a series of T2* images using the same TR scan time and a series of TE times. Subsequently, the T2* value of each pixel is calculated by selecting the appropriate regions of interest.

DeoxyHb increases the MR transverse relaxation rate (R2*) of water in blood and surrounding tissues thus BOLD-MRI is sensitive to pO2 within, and in tissues adjacent to perfused vessels [71].

The relation between T2* relaxation rate and R2* is that: R2*=1/ T2*.

V.2.b.II. BOLD imaging in cancer evaluation

Hypoxic cancers are more resistant to radiotherapy and chemotherapy. Currently there is interest in improving the therapeutic response of hypoxic cancers to radiotherapy by using radiosensitisers such as carbogen (95% oxygen mixed with 5% carbon dioxide to decrease oxygen induced vasoconstriction) [72].

Therefore,,there is a need for a non-invasive test that can identify hypoxic cancers which are likely to respond to this kind of treatment. BOLD uses a T2*-sensitive sequence during oxygen inhalation to detect an increase in signal resulting from the reduced paramagnetic effect of a reduction in the blood deoxyHb within a cancer. As with all functional MR techniques, BOLD presents challenges; the signal is not purely the result of oxygenation, the effects are short lived, and signal changes are small and may be difficult to reproduce. However, despite these difficulties BOLD has been used successfully to detect decreases in the blood deoxyHb in human cancers during carbogen inhalation [73, 74] and shows promise for tailoring treatment for hypoxic cancers

in the future. Indeed, hypoxia imaging may help select the most appropriate population that would benefit from novel hypoxia-directed therapies.

In clinical studies both native R2* and the change in R2* (ΔR2*) in response to oxygen/carbogen challenge have been used to estimate tumour hypoxia [74-77].

V.2.c. DCE-MR imaging

Perfusion is physiologically defined as the steady-state delivery of blood to an element of tissue [78]. Perfusion emphasizes more on the capillary blood blow and its contact with and irrigation through tissues rather than the luminal blood flow in the large blood vessels. Perfusion can be measured by various clinical imaging methods including MR. The advantages of MR perfusion include free- of-radiation, versatility and non-invasiveness possibility compared to other imaging modalities.

DCE-MR is most frequently used for oncological applications among perfusion MR methods to investigate various tissue properties such as the microstructure, permeability, tumour angiogenesis and hypoxia [79]. It describes the micro-vascular characteristics of tissue, such as blood flow/volume, surface area/permeability of vessel walls, and micro-vascular density. These characteristics are associated with the expression of potent cytokines (such as the vascular endothelial growth factor) that support the development of tumour vessels. This makes DCE-MRI a valuable diagnostic tool in oncology.

The basis of DCE-MR is rapid image acquisition to track the passage of a bolus injection of intravenous contrast through the tissue of interest, from which quantitative MR parameters are calculated, which reflect vascular flow and permeability. DCE-MR uses the dynamic transit of a paramagnetic contrast agent (gadolinium [Gd]-based, usually Gd-DTPA) administered intravenously.

Due to the T1-shortening effect after Gd-based contrast agent injection, the uptake and depletion of Gd by target tissue induces T1-weighted MR signal enhancement and reduction during the

perfusion procedure, which results in shortening the T1 relaxation time from its native value T10, and this temporal MR signal variation is recorded as voxel-wise time-intensity curves (TIC) by acquiring a series of dynamic MR images using a fast 2D/3D spoiled gradient echo sequence.

DCE-MR data can be analyzed qualitatively, semi- quantitatively or quantitatively. Qualitative DCE-MR analysis relies on the observation and categorization of TIC patterns to discriminate malignant and benign lesions. TICs of malignant lesions more frequently show a fast wash-in and fast wash-out TIC pattern which is associated with tumour neoangiogenesis [80]. TIC pattern analysis is widely used in breast cancer MRI and has been extended to HNC [80-84].

Semi-quantitative analysis of TIC can be conducted to derive various heuristic parameters to indicate the tissue perfusion property, such as bolus arrival time, time-to-peak, wash-in rate, wash-out rate and maximum enhancement [85]. Despite the advantages of straightforward and easy analysis, qualitative and semi- quantitative DCE-MR suffers from many limitations. For instance, semi-quantitative parameters can be remarkably affected by intrinsic tissue relaxation times, contrast agent registration protocol as well as imaging parameters.

Quantitative DCE-MR was thus proposed to overcome the above problems based on pharmacokinetic modelling of DCE-MR signal to set up the quantitative relationship between tissue properties and absolute contrast agent concentration in the tissue [86-87].

Quantitative analysis of the signal-time course can be performed by using a simple description of the enhancement curve or by fitting the data to an appropriate pharmacokinetic model to derive parameters that reflect tissue vascular perfusion/permeability (e.g. ktrans, kep) and extracellular volume fraction (ve) [88]. This requires knowledge of the arterial input function (AIF) which is either directly measured from a supplying artery or adopted from population values. As such, the conversion of TIC to time-concentration curve (TCC) from DCE-MR data is essential for quantitative DCE-MR, which requires a pre-contrast T1 measurement in DCE-MR acquisition. Among the various pharmacokinetic models proposed for DCE-MR, the Tofts model is most widely adopted [86, 89].

For the original Tofts model, three quantitative pharmacokinetic parameters of Ktrans, (the volume transfer constant between the blood plasma and extracellular extravascular space EES, wit unit of 1/min), kep (rate constant between EES and blood plasma, also with unit of 1/min) and ve (volume of EES per unit volume of tissue, ve = Ktrans/kep) could be derived. An additional parameter of vp (volume of blood plasma per unit volume of tissue) can be derived from the extended Tofts model. The ktrans value is dependent on both vascular perfusion and permeability. Ina flow-limited system (e.g. tumour tissue), ktrans will represent the blood plasma flow per unit volume of tissue. Whereas in a permeability limited system, the ktrans will represent the permeability surface area product per unit volume of tissue [90]. In the typical clinical scenario, using low molecular weight contrast such as Gd-DTPA to assess tumours, ktrans will predominantly indicate tumour perfusion. Despite the theoretical advantage of hardware and imaging protocol independence of quantitative pharmacokinetic parameters, it is still worth noting that the quantification of these parameters can be complicated and the quantified results can be considerably affected by many factors such as arterial input function (AIF) selection and measurement, T1 mapping, hardware imperfections (B0 and B1 inhomogeneity), hematocrit and model fitting algorithms [89]. In consequence, reproducibility of quantitative DCE-MR still needs to be further established through rigorous studies.

V.2.c.I. DCE-MR in H&N cancer evaluation

The merit and potential of DCE-MR have been reported by a number of studies for RT and/or CRT applications, mainly focused on prediction and early assessment of RT and CRT treatment response. Hoskin et al. [85] studied the correlation of pre- and post- treatment semi-quantitative DCE-MRI parameters and local tumour control after accelerated RT in HNCs. Cao et al. [91] found that the blood volume increase derived from the Tofts model in available primary tumour during the early course of RT was associated with local control, thus having potentials on intra-treatment modification. Shukla-Dave's study showed that skewness of Ktrans was the strongest

predictor of progression free survival (PFS) and overall survival (OS) in stage IV HNSCC patients with nodal disease, suggesting the importance of pre-treatment Ktrans as a predictor of treatment outcome [92]. Several other studies also reported that higher overall Ktrans or its increase was predictive of a good outcome following treatment in HNSCC [93-96].

As tumour vascularity could serve as a possible surrogate marker of hypoxia, DCE-MRI also has potential to reflect tumour hypoxia, which is attractive for adaptive and personalized radiotherapy treatment planning because hypoxia is a key factor to determine tumour resistance to treatment [97].

V.3. Summary of our results

Absolute ADC values for disease states and healthy tissues in general reflect a single predominant tissue feature (e.g. cellularity), but they are also influenced by other tissue characteristics (e.g. vascularity) and a number of technical factors relating to acquisition and processing of diffusion-weighted images. Our study utilized this multiple dependence and derived multi-scale ADC parameters for classification/identification of metastatic cervical lymph nodes in patients with head and neck SCC, and their difference with normal nodes.

We used 6 b-values and instead of applying a bi-exponential fit which would be prone to error, we explored the utility of two individual mono-exponential fits (3 b-values per mono-exponential) to separate perfusion and diffusion effects. Lowb-value (b0, 50 and 100s/mm2) images where signal loss reflected perfusion, and high b-value (b300, 600 and 1000s/mm2) where signal loss (from a baseline of b300) reflected extravascular water motion, were obtained in a single acquisition. Splitting into two groups (low b-value and high b-value) of monoexponential fits allowed derivation of ADCfast (perfusion) and ADCslow (diffusion). This approach provided a clinically

acceptable scan time of 4 to 5 minutes and an imaging volume encompassing the entire neck axially with 4 mm slice thickness and 1.6 x 1.6 mm image resolution.

We found significant differences between benign and metastatic nodes for median values of ADCfast, but not ADCslow, mirroring the discrepancy within existing literature. For example, Sumi et al [63] utilized b500 to 1000 images to calculate ADC analogous to our ADCslow measurement and found no difference between benign and metastatic nodes. In contrast, Razek et al [58] used a lowb-value (b<200) for their ADC calculation and, like our ADCfast measurements, found significant differences between benign and metastatic nodes. Our data support the theory that perfusion is reduced with disease, and that this reduction is an important determinant of observed ADC differences between these and benign nodes. Indeed, hypoxia combined with reduced perfusion in metastatic cervical nodes in patients with head and neck SCC has recently been observed using dynamic contrast enhanced MRI and positron emission tomography [102].

Our second major finding was that metastatic nodes could be identified by their histogram inter-voxel population distribution of ADC values. We found voxel populations of both ADC6b and ADCslow were positively skewed (i.e. greater number of voxels with low ADC values) in metastatic nodes compared with benign nodes. However, we found no such difference for ADCfast, and histograms remained positively skewed for both states. Considering that ADCfast and ADCslow reflect vascularity and cellularity respectively, histogram differences between metastatic and benign nodes may be ascribed to intravoxel structural changes of these histological features. The increased skewness of the ADCslow histogram (seen with metastatic nodes) may be interpreted as an increase in voxels with high cellularity.

Moreover the ADCfast histogram shape was quite different for metastatic nodes, compared with benign nodes, with a less spread of the values, result that together with the significantly lower median value of ADCfast of metastatic nodes than that for benign nodes, indicating a bulk shift in the histogram towards lower ADC, suggest global reduction in nodal perfusion in metastatic nodes.

We also investigated the stretched exponential model for discrimination between benign and metastatic nodes [12]. We found that the median α value of metastatic nodes was significantly greater than that for benign nodes, signifying reduced intra-voxel heterogeneity of diffusion rates in keeping with our dual mono-exponential results. To date there has been relatively little clinical application of the stretched exponential diffusion model, and no application in nodal disease. Kwee et al [103, 104] have investigated application in human gliomas and normal brain tissue, finding a reduced α value (increased intra-voxel diffusion heterogeneity) in tumor compared with normal tissue. Whilst this is contradictory to our observations in cervical nodes, it possibly reflects the different pathologies involved. Our α value is likely to reflect the diffusion rate heterogeneity caused by intravascular perfusion and extravascular diffusion processes existing within the same voxel.

Our study had some limitations. Sample size was predicated by available patients, but the fact our data were significant suggest they are valid. Our positive and negative nodal populations were differently sized, again reflecting available recruits. To counter this, we took great care to be certain regarding reference status for individual nodes by recruiting patients with N2/3 disease confirmed by CT, MRI and US ± FNA. Given our positive results, prospective application of our findings for identification of metastatic nodes of equal size distribution is being planned.

In summary, our results about DWI images suggest that the perfusion component of ADC estimates is the key parameter facilitating discrimination of metastatic from benign nodes in patients with head and neck SCC; and causes diffusion heterogeneity which is lost within metastatic nodes (producing α value differences between benign and metastatic nodes); and that the α value together with histogram features of ADC can provide a decision tree model for classification of nodal status.

About DCE images evaluation, PK parameters estimated with the proposed Bayesian inference algorithm had higher classification ability for head and neck metastatic nodes. PK parameters estimated with the simplex algorithm that could not significantly classify disease, when estimated

with the proposed Bayesian inference algorithm were significant classifiers of metastatic head and neck nodes (i.e. v_p and v_e). For the head and neck metastatic nodes only the ROC-AUC improvement of v_e was significant.

When run the simplex and the Bayesian inference algorithm for different initializations we found that the fitting error for the Bayesian inference algorithm was almost constant and consistently lower than the simplex algorithm for all initializations and for both populations.

The ROC-AUC of the PK parameters estimated with the Bayesian inference algorithms have an interquartile range equal to 0.01, whereas for the simplex algorithm the interquartile range is 0.23.

Bayesian inference algorithms have been proposed in the literature [98-100] to estimate unbiased quantitative PK parameters. The proposed scheme is similar to the one suggested by Schmid et al [98] the main differences are that the posterior probability distribution function $p(k,\sigma|C_{TIC})$ was parameterized with v_e to optimize EES volume directly instead of calculating it via k_{ep} ($v_e=K_{trans}/k_{ep}$). Moreover the accuracy of the estimated PK parameters depends on the arrival time of the contrast agent to the tissue (onset time) [101]. Wrong estimation of PK parameters can lead to big fitting errors. Orton et al [100] marginalized the onset time maximizing a marginal posterior distribution, whereas in this work onset time was included in the maximization process.

Finally, according to BOLD images evaluation, the observed reduction in T2* in metastatic lymph nodes suggests a paradoxical increase in deoxyhaemoglobin concentration on breathing 100% oxygen.

However, breathing 100% oxygen has multiple effects on body physiology, including a drop in the cardiac output and an increase in systemic resistance [105]. It is possible that the effect of these changes has a proportionally larger effect on blood flow to metastatic head and neck squamous cell cancer involved lymph nodes which already have an abnormal flow with absence of normal hilar vasculature [106]. The differential response to 100% oxygen inhalation between metastatic and normal nodes could potentially be exploited as a classifier of nodal disease status.

The observed results refute the initial study hypothesis of increment of T2* value after inhalation of 100% oxygen. Further work is needed to ascertain the mechanisms of paradoxical reduction in T2* found in metastatic head and neck squamous cell cancer lymph nodes on breathing 100% and to determine its potential utility for nodal status classification.

V.4. Methodological Limitations

There was a relatively small sample size. For this reason we took great care to be certain about positive and negative disease status within individual nodes by recruiting patients with N2/3 disease and healthy volunteers with benign nodes confirmed by CT, MRI and US ± FNA. N2/3 nodes ranged from 2 to 6 cm, whilst negative nodes ranged from 1 and 2 cm in short axis.

VI. CONCLUSIONS AND STUDY PERSPECTIVE

The present study shown important finding, indeed our results suggest that global reduction in nodal perfusion in metastatic nodes, and all these functional parameters evaluated (as DWI ADC_{fast} ability to differentiates malignant from benign nodes, as well as K_{trans} value), could potentially be exploited as classifier of nodal disease status, prior the starting of any types of therapy, and maybe in a next future be used to help the clinician in the choice of the more appropriate therapy for each patient.

New perspective of this work could be to enlarge the study population cohort, and take some follow-up MR examinations, using the same protocols, to check the status of the disease and any eventual change in nodal characteristics according to the response of the therapy.

VII. REFERENCES

1.Pryor DI, Solomon B, Porceddu SV. The emerging era of personalized therapy in squamous cell carcinoma of the head and neck. Asia Pac J Clin Oncol. 2011;7(3):236-51.

2.Brasilino de Carvalho M. Quantitative analysis of the extent of extracapsular invasion and its prognostic significance: a prospective study of 170 cases of carcinoma of the larynx and hypopharynx. Head Neck. 1998;20(1):16-21.

3.Byers RM, El-Naggar AK, Lee YY, et al. Can we detect or predict the presence of occult nodal metastases in patients with squamous carcinoma of the oral tongue? Head Neck. 1998;20(2):138-44.

4.Enepekides DJ, Sultanem K, Nguyen C, Shenouda G, Black MJ, Rochon L. Occult cervical metastases: immunoperoxidase analysis of the pathologically negative neck. Otolaryngol Head Neck Surg. 1999;120(5):713-7.

5.Tankere F, Camproux A, Barry B, Guedon C, Depondt J, Gehanno P. Prognostic value of lymph node involvement in oral cancers: a study of 137 cases. Laryngoscope. 2000;110(12):2061-5.

6.Esposito ED, Motta S, Cassiano B, Motta G. Occult lymph node metastases in supraglottic cancers of the larynx. Otolaryngol Head Neck Surg. 2001;124(3):253-7.

7.Coatesworth AP, MacLennan K. Squamous cell carcinoma of the upper aerodigestive tract: the prevalence of microscopic extracapsular spread and soft tissue deposits in the clinically N0 neck. Head Neck. 2002;24(3):258-61.

8.Suoglu Y, Erdamar B, Katircioglu OS, Karatay MC, Sunay T. Extracapsular spread in ipsilateral neck and contralateral neck metastases in laryngeal cancer. Ann Otol Rhinol Laryngol. 2002;111(5 Pt 1):447-54.

9.Greenberg JS, Fowler R, Gomez J, et al. Extent of extracapsular spread: a critical prognosticator in oral tongue cancer. Cancer. 2003;97(6):1464-70.

10.Woolgar JA, Rogers SN, Lowe D, Brown JS, Vaughan ED. Cervical lymph node metastasis in oral cancer: the importance of even microscopic extracapsular spread. Oral Oncol. 2003;39(2):130-7.

11.King AD. Multimodality imaging of head and neck cancer. Cancer Imaging. 2007 Oct 1;7 Spec No A:S37-46

12.Bennett KM, Schmainda KM, Bennett RT, Rowe DB, Lu H, Hyde JS. Characterization of continuously distributed cortical water diffusion rates with a stretched-exponential model. Magn Reson Med. 2003;50(4):727-34.

13.Sobin LH. TNM classification of malignant tumours. 7 ed. Chichester, West Sussex, UK ; Hoboken, NJ: John Wiley and Sons, 2009.

14. Dikaios N, Punwani S, Hamy V, Purpura P, Rice S, Forster M, Mendes R, Taylor S, Atkinson D. Noise estimation from averaged diffusion weighted images: Can unbiased quantitative decay parameters assist cancer evaluation? Magn Reson Med. 2014;71: 2105-17.

15.Hanley JA, McNeil BJ. The meaning and use of the area under a Receiver Operating Characteristic (ROC) curve. Radiology, 1982, 143, 29-36.

16.Jemal A, Bray F, Center MM, et al. Global cancer statistics. CA Cancer J Clin 2011; 61:69.

17.Chaturvedi AK, Anderson WF, Lortet-Tieulent J, et al. Worldwide trends in incidence rates for oral cavity and oropharyngeal cancers. J Clin Oncol 2013; 31:4550

18.Ferlay J, Shin HR, Bray F, et al. Estimates of worldwide burden of cancer in 2008: GLOBOCAN 2008. Int J Cancer 2010; 127:2893

19.Vokes, E. E., Weichselbaum, R. R., Lippman, S. M., Hong, W. K., 1993. Head and neck cancer. New England Journal of Medicine 328 (3), 184–194.

20.Snow, G., Annyas, A., Slooten, E. v., Bartelink, H., Hart, A., 1982. Prognostic factors of neck node metastasis. Clinical Otolaryngology & Allied Sciences 7 (3), 185–192.

21.Som, P. M., Curtin, H. D., Mancuso, A. A., 2000. Imaging-based nodal classification for evaluation of neck metastatic adenopathy. American Journal of Roentgenology 174 (3), 837–844

22.Farr HW, Goldfarb PM, Farr CM. Epidermoid carcinoma of the mouth and pharynx at Memorial Sloan-Kettering Cancer Center, 1965-1969. Am J Surg. 1980;140(4):563–7

23.Spiro RH. The management of neck nodes in head and neck cancer: a surgeon's view. Bull N Y Acad Med. 1985;61(7): 629–37

24.van den Brekel MW, Stel HV, Castelijns JA, et al. Cervical lymph node metastasis: assessment of radiologic criteria. Radiology. 1990;177(2):379–84.

25.van den Brekel MW, Bartelink H, Snow GB. The value of staging of neck nodes in patients treated with radiotherapy. Radiother Oncol. 1994;32(3):193–6

26.Robbins KT, Clayman G, Levine PA, et al. Neck dissection classification update: revisions proposed by the American Head and Neck Society and the American Academy of Otolaryngology-Head and Neck Surgery. Arch Otolaryngol Head Neck Surg. 2002;128:751–8.

27.Som PM. Detection of metastasis in cervical lymph nodes: CT and MR criteria and differential diagnosis. AJR Am J Roentgenol 1992;158:961–969

28.Steinkamp HJ, Hosten N, Richter C, Schedel H, Felix R. Enlarged cervical lymph nodes at helical CT. Radiology 1994;191:795–798

29.Vassallo P, Wernecke K, Roos N, Peters PE. Differentiation of benign from malignant superficial lymphadenopathy: the role of high-resolution US. Radiology 1992;183:215–220

30.Choi MY, Lee JW, Jang KJ. Distinction between benign and malignant causes of cervical, axillary, and inguinal lymphadenopathy: value of Doppler spectral waveform analysis. AJR Am J Roentgenol 1995;165:981–984

31.Anzai Y, Brunberg JA, Lufkin RB. Imaging of nodal metastases in the head and neck. J Magn Reson Imaging 1997;7:774–783

32.Bussink J, van Herpen CM, Kaanders JH, Oyen WJ. PET-CT for response assessment and treatment adaptation in head and neck cancer. Lancet Oncol 2010;11(7):661–669

33.Nordsmark M, Bentzen SM, Rudat V, et al. Prognostic value of tumor oxygenation in 397 head and neck tumors after primary radiation therapy: an international multi-center study. Radiother Oncol 2005;77(1):18–24

34.Hall EJ, Giaccia AJ. Oxygen effect and reoxygenation. In: Hall EJ, Giaccia AJ, eds. Radiobiology for the radiologist. Philadelphia, Pa: Lippincott Williams & Wilkins, 2006; 85–105

35.Merboldt KD, Hanicke W, Frahm J. Diffusion imaging using stimulated echoes. Magn Reson Med. 1991 Jun;19(2):233-9.

36.Taylor DG; Bushell MC. The spatial mapping of translational diffusion coefficients by the NMR imaging technique. Physics in Medicine and Biology. 1985; 30 (4): 345–349

37.Le Bihan D, Breton E, Lallemand D, Grenier P, Cabanis E, Laval-Jeantet M. MR imaging of intravoxel incoherent motions: application to diffusion and perfusion in neurologic disorders. Radiology 1986; 161:401–407.

38.Stejskal EO, Tanner JE. Spin diffusion measurements: spin-echo in the presence of a time dependent field Gradient. J Chem Phys 1965; 42:288–292.

39. Patterson DM, Padhani AR, Collins DJ. Technology insight: water diffusion MRI—a potential new biomarker of response to cancer therapy. Nat Clin Pract Oncol 2008; 5:220–233.

40.Quayuum A. Diffusion-weighted imaging in the abdomen and pelvis: concepts and applications. Radiographics 2009; 29:1797 -1810.

41.Thoeny HC, De Keyzer F. Extracranial applications of diffusion-weighted magnetic resonance imaging. Eur Radiol 2007; 17:1385–1393.

42.Koh DM, Collins DJ. Diffusion-weighted MRI in the body: applications and challenges in oncology. Am J Roentgenol 2007; 188:1622–1635.

43.Schwarz A, Bogner P, et al. The exsistence of bioexponential signal decay in magnetic resonance diffusion-weighted imaging appears to be independent of compartimentalization. Magnetic Resonance Medicine 2004; 51:278-285.

44.Le Bihan D, Breton E, Lallemand D Aubin ML, et al. Separation of diffusion and perfusion in intravoxel incoherent motion MR imaging. Radiology1988; 168:497-505.

45.Padhani AR, Liu G, Koh DM, et al. Diffusion-weighted magnetic resonance imaging as a cancer biomarker: consensus and recommendations. Neoplasia 2009;11:102–125.

46.Jung F, Mrowietz C, Hiebl B, Franke RP, Pindur G, Sternitzky R. Influence of rheological parameters on the velocity of erythrocytes passing nailfold capillaries in humans. Clin Hemorheol Microcirc. 2011;48(1):129-39.

47.Chenevert TL, Galban CJ, Ivancevic MK, et al. Diffusion coefficient measurement using a temperature-controlled fluid for quality control in multicenter studies. J Magn Reson Imaging. 2011;34(4):983-7.

48.Kallehauge JF, Tanderup K, Haack S, et al. Apparent Diffusion Coefficient (ADC) as a quantitative parameter in diffusion weighted MR imaging in gynecologic cancer: Dependence on b-values used. Acta Oncol. 2010;49(7):1017-22.

49.Xing D, Papadakis NG, Huang CL, Lee VM, Carpenter TA, Hall LD. Optimised diffusion-weighting for measurement of apparent diffusion coefficient (ADC) in human brain. Magn Reson Imaging. 1997;15(7):771-84.

50.Lemke A, Stieltjes B, Schad LR, Laun FB. Toward an optimal distribution of b values for intravoxel incoherent motion imaging. Magn Reson Imaging. 2011;29(6):766-76.

51.Wang J, Takashima S, Takayama F, Kawakami S, Saito A, Matsushita T, Momose M, Ishiyama T. Head and neck lesions: characterization with diffusion-weighted echo-planar MR imaging. Radiology 2001; 220:621-623.

52.Maeda M, Maier SE. Usefulness of diffusion-weighted imaging apparent diffusion coefficient in the assessment of head and neck tumors. J Neuroradiology 2008; 35:71-78.

53.Chawla S, Kim S, Wang S, Poptani H. Diffusion-weighted imaging in head and neck cancers. Future Oncol 2009;Sep;5(7):959-75. doi: 10.2217/fon.09.77.

54.Koç O, Paksoy Y, Erayman I, Kivrak AS, Arbag H. Role of diffusion weighted MR in the discrimination diagnosis of the cystic and/or necrotic head and neck lesions. Eur J Radiol 2007; 62:205-213.

55.Hermans R, Vandecaveye V. Diffusion weighted imaging MRI in head and neck cancer. JBR 2007; 90:264-267.

56.Srinivasan A, Dvorak R, Perni K, Rohrer S, Mukherji SK. Differentiation of benign and malignant pathology in the head and neck using 3T apparent diffusion coefficient values: early experience. AJNR Am J Neuroradiol 2008;29: 40-44

57.Vandecaveye V, De Keyzer F, Vander Poorten V, et al. Head and neck squamous cell carcinoma: value of diffusion-weighted MR imaging for nodal staging. Radiology. 2009;251(1):134-46.

58.Abdel Razek AA, Soliman NY, Elkhamary S, Alsharaway MK, Tawfik A. Role of diffusion-weighted MR imaging in cervical lymphadenopathy. Eur Radiol. 2006;16(7):1468-77.

59.de Bondt RB, Hoeberigs MC, Nelemans PJ, et al. Diagnostic accuracy and additional value of diffusion-weighted imaging for discrimination of malignant cervical lymph nodes in head and neck squamous cell carcinoma. Neuroradiology. 2009;51(3):183-92.

60.Perrone A, Guerrisi P, Izzo L, et al. Diffusion-weighted MRI in cervical lymph nodes: differentiation between benign and malignant lesions. Eur J Radiol. 2011;77(2):281-6.

61.Holzapfel K, Duetsch S, Fauser C, Eiber M, Rummeny EJ, Gaa J. Value of diffusion-weighted MR imaging in the differentiation between benign and malignant cervical lymph nodes. Eur J Radiol. 2009;72(3):381-7.

62.Sumi M, Sakihama N, Sumi T, et al. Discrimination of metastatic cervical lymph nodes with diffusion-weighted MR imaging in patients with head and neck cancer. AJNR Am J Neuroradiol. 2003;24(8):1627-34.

63.Sumi M, Van Cauteren M, Nakamura T. MR microimaging of benign and malignant nodes in the neck. AJR Am J Roentgenol. 2006;186(3):749-57.

64.Tozer DJ, Jager HR, Danchaivijitr N, et al. Apparent diffusion coefficient histograms may predict low-grade glioma subtype. NMR Biomed. 2007;20(1):49-57.

65.Khayal IS, Nelson SJ. Characterization of low-grade gliomas using RGB color maps derived from ADC histograms. J Magn Reson Imaging. 2009;30(1):209-13.

66.Gasparotti R, Pinelli L, Liserre R. New MR sequences in daily practice: susceptibility weighted imaging. A pictorial essay. Insights Imaging. 2011 Jun; 2(3): 335–347. doi: 10.1007/s13244-011-0086-3

67.Raichle ME. Behind the scenes of functional brain imaging: a historical and physiological perspective. Proc Natl Acad Sci. 1998;95:765–772.

68.Kim YR, Huang IJ, Lee SR, et al. Measurements of BOLD/CBV ratio show altered fMRI hemodynamics during stroke recovery in rats. J Cereb Blood Flow Metab. 2005;25:820–829.

69.Leontiev O, Buxton RB. Reproducibility of BOLD, perfusion, and CMRO2 measurements with calibrated-BOLD fMRI. Neuroimage. 2007;35:175–184.

70.Padhani AR, Krohn KA, Lewis JS, Alber M. Imaging oxygenation of human tumours. Eur Radiol. 2007 Apr;17(4):861-72. Review.

71.Howe FA, Robinson SP, McIntyre DJ, Stubbs M, Griffiths JR (2001) Issues in flow and oxygenation dependent contrast (FLOOD) imaging of tumours. NMR Biomed 14:497–506

72.Kaanders JHAM, Pop LAM, Marres HAM, et al. ARCON: experience in 215 patients with advanced head and neck cancer. Int J Radiat Oncol Biol Phys 2002; 52: 260_3

73.Griffiths JR, Taylor NJ, Howe FA, et al. The response of human tumors to carbogen breathing, monitored by gradient-recalled echo magnetic resonance imaging. Int J Radiat Oncol Biol Phys 1997; 39: 697_701.

74.Rijpkema M, Kaanders JHAM, Joosten FBM, van der Kogel AJ, Heerschap A. Effects of breathing hyperoxic hypercapnic gas mixture on blood oxygenation and vascularity of head-and-neck tumors as measured by magnetic resonance imaging. Int J Radiat Oncol Biol Phys 2002; 53: 1185_91

75.Alonzi R, Padhani AR, Maxwell RJ, Taylor NJ, Stirling JJ, Wilson JI, d'Arcy JA, Collins DJ, Saunders MI, Hoskin PJ. Carbogen breathing increases prostate cancer oxygenation: a translational MRI study in murine xenografts and humans. Br J Cancer. 2009 Feb 24;100(4):644-8. doi: 10.1038/sj.bjc.6604903.

76.Hallac RR, Ding Y, Yuan Q, McColl RW, Lea J, Sims RD, Weatherall PT, Mason RP. Oxygenation in cervical cancer and normal uterine cervix assessed using blood oxygenation level-dependent (BOLD) MRI at 3T. NMR Biomed. 2012 Dec;25(12):1321-30. doi: 10.1002/nbm.2804.

77.Kotas M, Schmitt P, Jakob PM, Flentje M. Monitoring of tumor oxygenation changes in head-and-neck carcinoma patients breathing a hyperoxic hypercapnic gas mixture with a noninvasive MRI technique. Strahlenther Onkol. 2009 Jan;185(1):19-26. doi: 10.1007/s00066-009-1870-6.

78.Essig M, Shiroishi MS, Nguyen TB, Saake M, Provenzale JM, Enterline D, Anzalone N, Dorfler A, Rovira A, Wintermark M, Law M. Perfusion MRI: the five most frequently asked technical questions. AJR Am J Roentgenol 2013;200:24-34.

79.Tofts PS, Kermode AG. Measurement of the blood-brain barrier permeability and leakage space using dynamic MR imaging. 1. Fundamental concepts. Magn Reson Med 1991;17:357-67

80.Kuhl CK, Mielcareck P, Klaschik S, Leutner C, Wardelmann E, Gieseke J, Schild HH. Dynamic breast MR imaging: are signal intensity time course data useful for differential diagnosis of enhancing lesions? Radiology 1999;211:101-10

81.Weinstein D, Strano S, Cohen P, Fields S, Gomori JM, Degani H. Breast fibroadenoma: mapping of pathophysiologic features with three-time-point, contrast-enhanced MR imaging--pilot study. Radiology 1999;210:233-40.

82.Asaumi J, Yanagi Y, Hisatomi M, Matsuzaki H, Konouchi H, Kishi K. The value of dynamic contrast-enhanced MRI in diagnosis of malignant lymphoma of the head and neck. Eur J Radiol 2003;48:183-7.

83.Sumi M, Nakamura T. Extranodal spread in the neck: MRI detection on the basis of pixel-based time-signal intensity curve analysis. J Magn Reson Imaging 2011;33:830-8.

84.Yuan J, Chow SK, Yeung DK, King AD. A five-colour colour-coded mapping method for DCE-MRI analysis of head and neck tumours. Clin Radiol 2012;67:216-23

85.Hoskin PJ, Saunders MI, Goodchild K, Powell ME, Taylor NJ, Baddeley H. Dynamic contrast enhanced magnetic resonance scanning as a predictor of response to accelerated radiotherapy for advanced head and neck cancer. Br J Radiol 1999;72:1093-8

86.Tofts PS, Brix G, Buckley DL, Evelhoch JL, Henderson E, Knopp MV, Larsson HB, Lee TY, Mayr NA, Parker GJ, Port RE, Taylor J, Weisskoff RM. Estimating kinetic parameters from dynamic contrast-enhanced T(1)-weighted MRI of a diffusable tracer: standardized quantities and symbols. J Magn Reson Imaging 1999;10:223-32.

87.Tofts PS. Modeling tracer kinetics in dynamic Gd-DTPA MR imaging. J Magn Reson Imaging 1997;7:91-101.

88.Zahra MA, Hollingsworth KG, Sala E, Lomas DJ, Tan LT. Dynamic contrast-enhanced MRI as a predictor of tumour response to radiotherapy. Lancet Oncol 2007;8:63-74

89.Sourbron SP, Buckley DL. On the scope and interpretation of the Tofts models for DCE-MRI. Magn Reson Med 2011;66:735-45.

90.O'Connor JPB, Jackson A, Parker GJM, Jayson GC. DCE-MRI biomarkers in the clinical evaluation of antiangiogenic and vascular disrupting agents. Br J Cancer 2007;96:189-95

91.Cao Y, Popovtzer A, Li D, Chepeha DB, Moyer JS, Prince ME, Worden F, Teknos T, Bradford C, Mukherji SK, Eisbruch A. Early prediction of outcome in advanced head-and-neck cancer based on tumor blood volume alterations during therapy: a prospective study. Int J Radiat Oncol Biol Phys 2008;72:1287-90.

92.Shukla-Dave A, Lee NY, Jansen JF, Thaler HT, Stambuk HE, Fury MG, Patel SG, Moreira AL, Sherman E, Karimi S, Wang Y, Kraus D, Shah JP, Pfister DG, Koutcher JA. Dynamic contrast-enhanced magnetic resonance imaging as a predictor of outcome in head-and-neck squamous cell carcinoma patients with nodal metastases. Int J Radiat Oncol Biol Phys 2012;82:1837-44.

93.Kim S, Loevner LA, Quon H, Kilger A, Sherman E, Weinstein G, Chalian A, Poptani H. Prediction of response to chemoradiation therapy in squamous cell carcinomas of the head and neck using dynamic contrast-enhanced MR imaging. AJNR Am J Neuroradiol 2010;31:262-8.

94.Chawla S, Kim S, Loevner LA, Hwang WT, Weinstein G, Chalian A, Quon H, Poptani H. Prediction of diseasefree survival in patients with squamous cell carcinomas of the head and neck using dynamic contrast-enhanced MR imaging. AJNR Am J Neuroradiol 2011;32:778-84.

95.Chikui T, Kitamoto E, Kawano S, Sugiura T, Obara M, Simonetti AW, Hatakenaka M, Matsuo Y, Koga S, Ohga M, Nakamura K, Yoshiura K. Pharmacokinetic analysis based on dynamic contrast-enhanced MRI for evaluating tumor response to preoperative therapy for oral cancer. J Magn Reson Imaging 2012;36:589-597.

96.Ng SH, Lin CY, Chan SC, Yen TC, Liao CT, Chang JT, Ko SF, Wang HM, Huang SF, Lin YC, Wang JJ. Dynamic contrast-enhanced MR imaging predicts local control in oropharyngeal or hypopharyngeal squamous cell carcinoma treated with chemoradiotherapy. PLoS One 2013;8:e72230.).

97.Janssen HL, Haustermans KM, Balm AJ, Begg AC. Hypoxia in head and neck cancer: How much, how important? Head Neck 2005;27:622-38.

98.Schmid V, Witcher B, Padhani A, Taylor N and Yang G-Z 2006 Bayesian methods for pharmacokinetic models in dynamic constrast-enhanced magnetic resonance imaging IEEE Trans. Med. Imaging 25 1627–36.

99.Bhushan M, Schnabel JA, Risser L, Heinrich MP, Brady JM, Jenkinson M. Motion correction and parameter estimation in dceMRI sequences: application to colorectal cancer. Med Image Comput Comput Assist Interv. 2011;14:476-83.

100.Orton MR, Collins DJ, Walker-Samuel S, d'Arcy JA, Hawkes DJ, Atkinson D, Leach MO. Bayesian estimation of pharmacokinetic parameters for DCE-MRI with a robust treatment of enhancement onset time. Phys Med Biol. 2007 May 7; 52(9):2393-408.

101.Calamante F, Gadian D and Connelly A. Delay and dispersion effects in dynamic susceptibility contrast MRI: simulations using singular value decomposition Magn. Reson. Med. 200; 44: 466–73

102.Jansen JF, Schoder H, Lee NY, et al. Noninvasive assessment of tumor microenvironment using dynamic contrast-enhanced magnetic resonance imaging and 18F-fluoromisonidazole positron emission tomography imaging in neck nodal metastases. Int J Radiat Oncol Biol Phys. 2010;77(5):1403-10.

103.Kwee TC, Galban CJ, Tsien C, et al. Comparison of apparent diffusion coefficients and distributed diffusion coefficients in high-grade gliomas. J Magn Reson Imaging. 2010;31(3):531-7.

104.Kwee TC, Galban CJ, Tsien C, et al. Intravoxel water diffusion heterogeneity imaging of human high-grade gliomas. NMR Biomed. 2010;23(2):179-87.

105.Daly W, Bondurant S. Effects of oxygen breathing on the heart rate, blood pressure and cardiac index of normal men-resting, with reactive hyperemia, and after atropine. Journal of Clinical Investigation Vol. 41, No. 1, 1962

106.Yonetsu K, Sumi M, Izumi M, Ohki M, Eida S, Nakamura T. Contribution of doppler sonography blood flow information to the diagnosis of metastatic cervical nodes in patients with head and neck cancer: assessment in relation to anatomic levels of the neck. AJNR Am J Neuroradiol. 2001 Jan;22(1):163-9.

VIII. TABLES

Table 1. MRI Sequence Parameters.

Parameter	Axial PROPELLER	Axial STIR-EPI DWI	Coronal DCE	Axial BOLD
No. of sections	60	42	33	27
Stacks	1-2*	1	1	1
Field of view	20 cm	20 cm	269 mm	20 cm
Repetition time (msec)	6310	8700	2.3	1450
Echo time (msec)	107	88	1.0	12, 24, 36 and 48
Inversion time (msec)	n/a	180	n/a	n/a
Matrix	256 x 256	128 x 128	176 x 256	256 x 256
Section thickness (mm)	3	4	4	4
Section gap (mm)	0.3	0.4	0.3	0.4
Averages	1	4	1	4
Echo train	29	n/a	11	n/a
Parallel acquisition	2	2	2	2
b-values (s/mm^2)	n/a	0, 50, 100, 300, 600 and 1000	n/a	n/a

* variable dependent of patient size

PROPELLER - Periodically Rotated Overlapping ParallEL Lines with Enhanced Reconstruction

STIR – Short Tau Inversion Recovery

EPI – Echo Planar Imaging

DWI – Diffusion Weighted Imaging

DCE – Dynamic Contrast Enhanced

BOLD – Blood oxygenation level dependent

Table 2. Patient demographics.

Patient No.	Primary Tumour Site	Stage
1	Soft Palate/ Oropharynx	T2 N2c M0
2	Tonsil	T1 N3 M0
3	Tonsil	T2 N2c M0
4	Tonsil	T1 N2b M0
5	Tongue Base	T4 N2c M0
6	Tonsil	T2 N2b M0
7	Pyriform Fossa	T3 N2b M0
8	Oropharynx	T1 N2b M0
9	Pyriform Fossa	T2 N2b M0
10	Unknown	Tx N2a M0
11	Oropharynx	T2 N2b M0
12	Tonsil	T3 N2b M0
13	Tonsil	T2 N2b M0
14	Tonsil/Glossotonsillar fossa	T1 N2b M0
15	Oropharynx	T4 N2c M0
16	Tongue Base/ Oropharynx	T3 N2c Mx
17	Oropharynx	T4 N2c M0
18	Tonsil	T4 N2b M0
19	Base Tongue	T2 N2b M0
20	Oropharynx	T3 N2b M0
21	Unknown	Tx N2c M0
22	Epiglottis	T2N2b M0/M1
23	Tonsil	T4 N2b M0
24	Tonsil	T2 N2b Mx/M0

N2a – single > 3cm but ≤ 6cm in greatest dimension

N2b – metastases in multiple ipsilateral nodes < 6cm

N3 – node > 6cm

Table 3. Benign verses metastatic volumetric ROI analysis.

Median Parameter Value	Benign Cervical Node	Metastatic Cervical Node	p-value
ADC_{6b} ($x10^{-3}mm^2/s$)	1.0	1.04	0.1575
ADC_{slow} ($x10^{-3}mm^2/s$)	0.98	1.04	0.0982
ADC_{fast} ($x10^{-3}mm^2/s$)	1.76	1.56	0.0458*
DDC ($x10^{-3}mm^2/s$)	0.79	0.87	0.0513
Stretched exponential α value	0.73	0.77†	0.026*

* significant difference between benign and metastatic parameter at the $p<0.05$ level

ADC_{6b} – apparent diffusion coefficient derived from mono-exponential fit using 6 b values (0, 50, 100, 300, 600 and 1000 s/mm^2)

ADC_{slow} – apparent diffusion coefficient derived from mono-exponential fit using 3 lowest b values (0, 50 and 100 s/mm^2) - reflecting perfusion

ADC_{fast} – apparent diffusion coefficient derived from mono-exponential fit using 3 higest b values (300, 600 and 1000 s/mm^2) - eliminating perfusion

DDC – apparent diffusion coefficient derived from a stretched exponential fit using 6 b values (0, 50, 100, 300, 600 and 1000 s/mm^2)

ROI – region of interest

† – individual values normally distributed across patients

Table 4. Benign versus metastatic histogram population distribution analysis.

Median Parameter Value	Benign Cervical Node	Metastatic Cervical Node	p-value
Skewness of ADC_{6b}	1.151	1.647	0.0028*
Skewness of ADC_{slow}	0.3936†	0.9835	< 0,0001*
Skewness of ADC_{fast}	0.7731†	0.9928	0.095
Skewness of DDC	1.046	1.573	0.0055*
Skewness of α value	-0.0817	-0.1767†	0.1167

* significant difference between benign and metastatic parameter at the $p<0.05$ level

ADC_{6b} – apparent diffusion coefficient derived from mono-exponential fit using 6 b values (0, 50, 100, 300, 600 and 1000 s/mm^2)

ADC_{slow} – apparent diffusion coefficient derived from mono-exponential fit using 3 lowest b values (0, 50 and 100 s/mm^2) - reflecting perfusion

ADC_{fast} – apparent diffusion coefficient derived from mono-exponential fit using 3 highest b values (300, 600 and 1000 s/mm^2) - eliminating perfusion

DDC – apparent diffusion coefficient derived from a stretched exponential fit using 6 b values (0, 50, 100, 300, 600 and 1000 s/mm^2)

† – individual values normally distributed across patients

Table 5. Score test and univariate analysis of the PK parameters derived using the simplex and the Bayesian inference algorithm performed on the whole head and neck node population and following LOO analysis.

		score (p-value)	ROC AUC (CI)	LOO ROC-AUC (CI)
simplex	v_p	0.41 (0.52)	0.53 (0.42-0.64)	0.40 (0.29-0.50)
	K_{trans}	28.94 (<0.01)	0.79 (0.70-0.88)	0.73 (0.63-0.84)
	v_e	0.47 (0.49)	0.53 (0.42-0.65)	0.40 (0.29-0.52)
Bayesian	v_p	4.60 (0.03)	0.58 (0.47-0.68)	0.52 (0.41-0.63)
	K_{trans}	29.34 (<0.01)	0.81 (0.71-0.89)	0.77 (0.68-0.87)
	v_e^*	16.85 (<0.01)	0.74 (0.70-0.88)	0.72 (0.62-0.82)

Asterisk (*) denotes the cases where the PK parameter estimated with the Bayesian inference algorithm is significantly different than the corresponding one derived with the simplex algorithm.

Table 6. Median ROC-AUC and interquartile range (iQR) of the PK parameters derived with the simplex and the Bayesian inference algorithm using different initializations performed on the head and neck population.

		Median ROC-AUC	iQR
simplex	v_p	0.62	0.09
	K_{trans}	0.74	0.06
	v_e	0.66	0.19
Bayesian	v_p^*	0.56	0.03
	K_{trans}	0.78	<0.01
	v_e	0.74	<0.01

Asterisk (*) denotes the cases where the PK parameter estimated with the Bayesian inference algorithm is significantly different than the corresponding one derived with the simplex algorithm.

Table 7. Histographic T2* parameters for metastatic and normal lymph nodes derived from T2* maps acquired with participants on room air and 100% oxygen.

	Metastatic Nodes (n=60)			Normal nodes (n=18)		
	Mean of T2* histogram median values (ms)	Mean of T2* histogram skewness	Mean of T2* histogram kurtosis	Mean of T2* histogram median values (ms)	Mean of T2* histogram skewness	Mean of T2* histogram kurtosis
ON ROOM AIR	47.0	0.31	-0.12	43.9	0.73	0.22
ON 100% OXYGEN	33.2	0.55	0.15	47.0	0.95	0.85
Paired t-test p-value	<0.001*	0.002*	0.005*	0.148	0.136	0.160

Table 8. Generic staging for head and neck cancer.

Primary tumor	
Tis or (T0)	Carcinoma *in situ*
T1	Tumour < 2 cm
T2	Tumour > 2-4 cm
T3	Tumour > 4 cm
T4	Tumour involves adjacent structures
T4a	Operable disease
T4b	Inoperable disease
Nodes	Spread of cancer to lymph nodes
N0	No regional nodes metastasis
N1	Single ipsilateral node metastasis < 3 cm
N2a	Single ipsilateral node metastasis > 3-6 cm
N2b	Multiple ipsilateral node metastasis < 6 cm
N2c	Bilateral or contralateral < 6 cm
N3	Lymph node metastatis > 6 cm
Metastasis	Spread of tumor beyond lymph nodes to other parts of body
M0	No distant metastasis
M1	Metastasis to distant organs

IX. FIGURES

Figure 1. Axial Periodically Rotated Overlapping ParallEL Lines with Enhanced Reconstruction (PROPELLER) T2 image demonstrating a metastatic cervical node with multiple areas of necrosis (arrowheads).

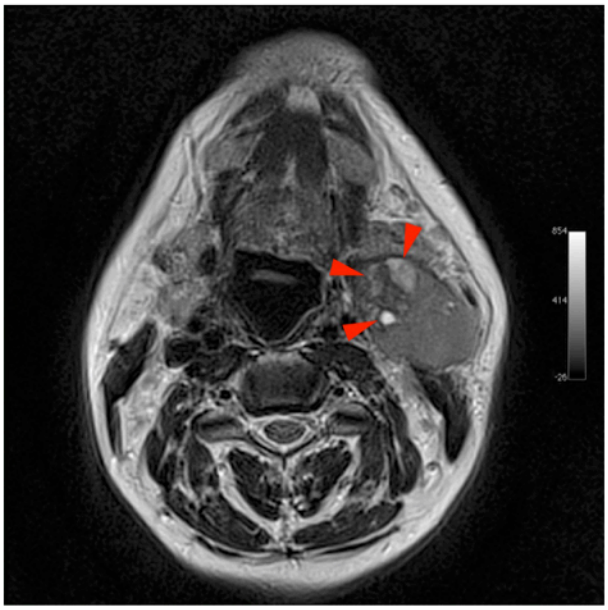

Figure 2. Axial Short Tau Inversion Recovery – Echo Planar Imaging (STIR-EPI) DWI of a metastatic cervical node with b-values of 0, 50, 100, 300, 600 and 1000 s/mm^2 demonstrating signal evolution with increasing diffusion weighting.

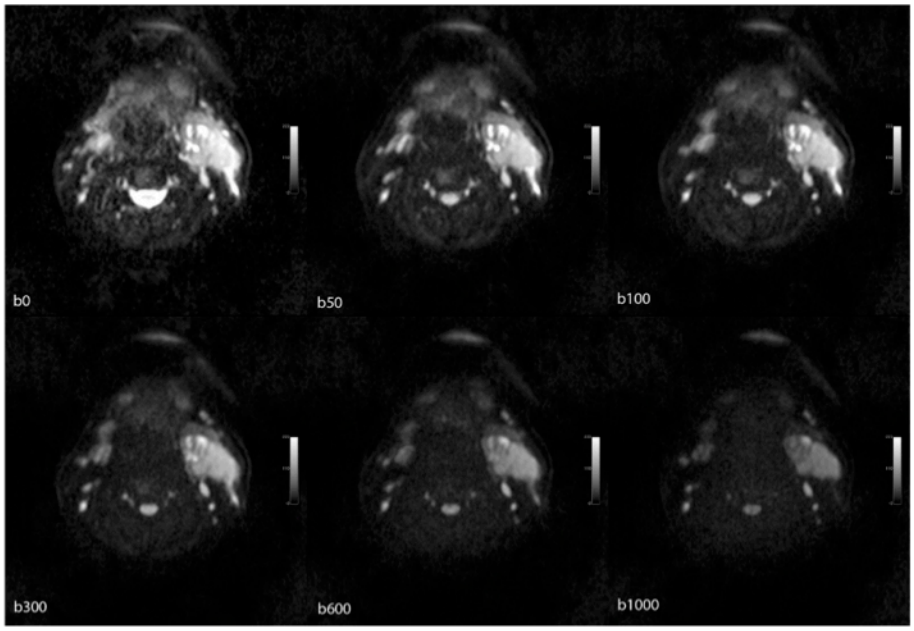
b0
b50
b100
b300
b600
b1000

Figure 3. Axial BOLD – T2* multi-echo GRE MRI images on air at 4 different echo times (12, 24, 36 and 48 ms) demonstrating signal evolution of bilateral nodes metastasis.

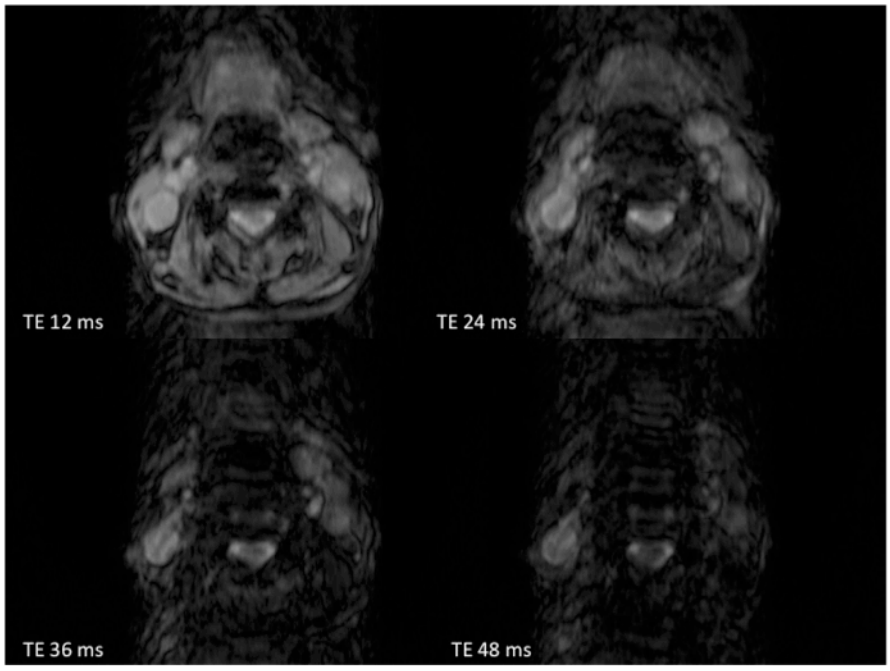

Figure 4. Quantitative parametric diffusion maps of (a) ADC6b, (b) ADCfast, (c) ADCslow, (d) DDC and (e) stretched exponential α value. Arrowhead indicates the metastatic left cervical lymph node. (ADC – apparent diffusion coefficient, DDC – distributed diffusion coefficient).

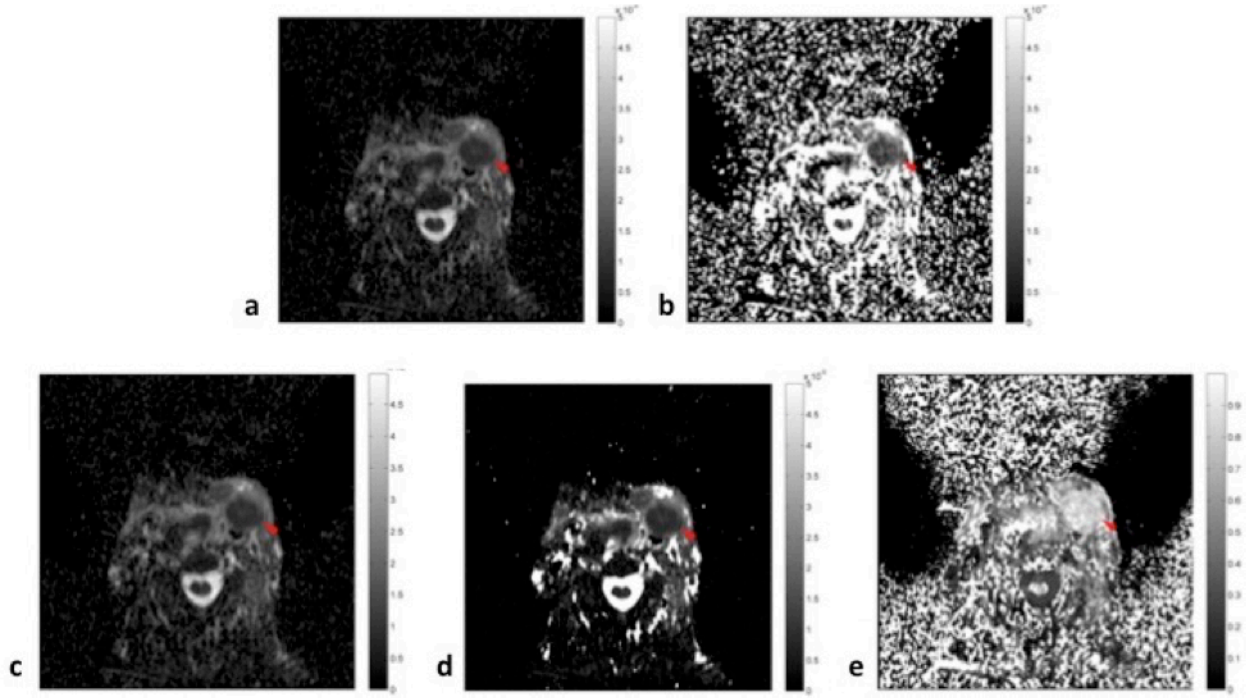

Figure 5. Colour T2* map on air (left) and on O2 (right) images demonstrating an enlarged left cervical lymph node.

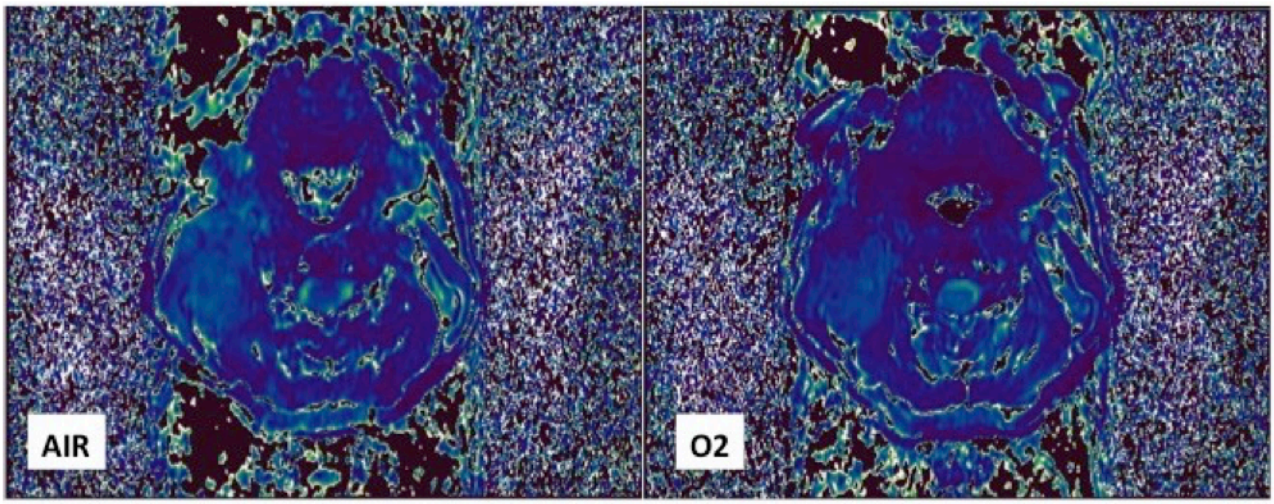

Figure 6. Parametric PK maps (v_p, K_{trans}, v_e) estimated with pixel-by-pixel fitting using the simplex and the Bayesian inference algorithm for a head and neck node with metastasis. A plot of the mean ROI concentration profile $C_{TIC}(t)$ and the fitted to $C_{TIC}(t)$ curve using the simplex and the Bayesian inference algorithm is also shown.

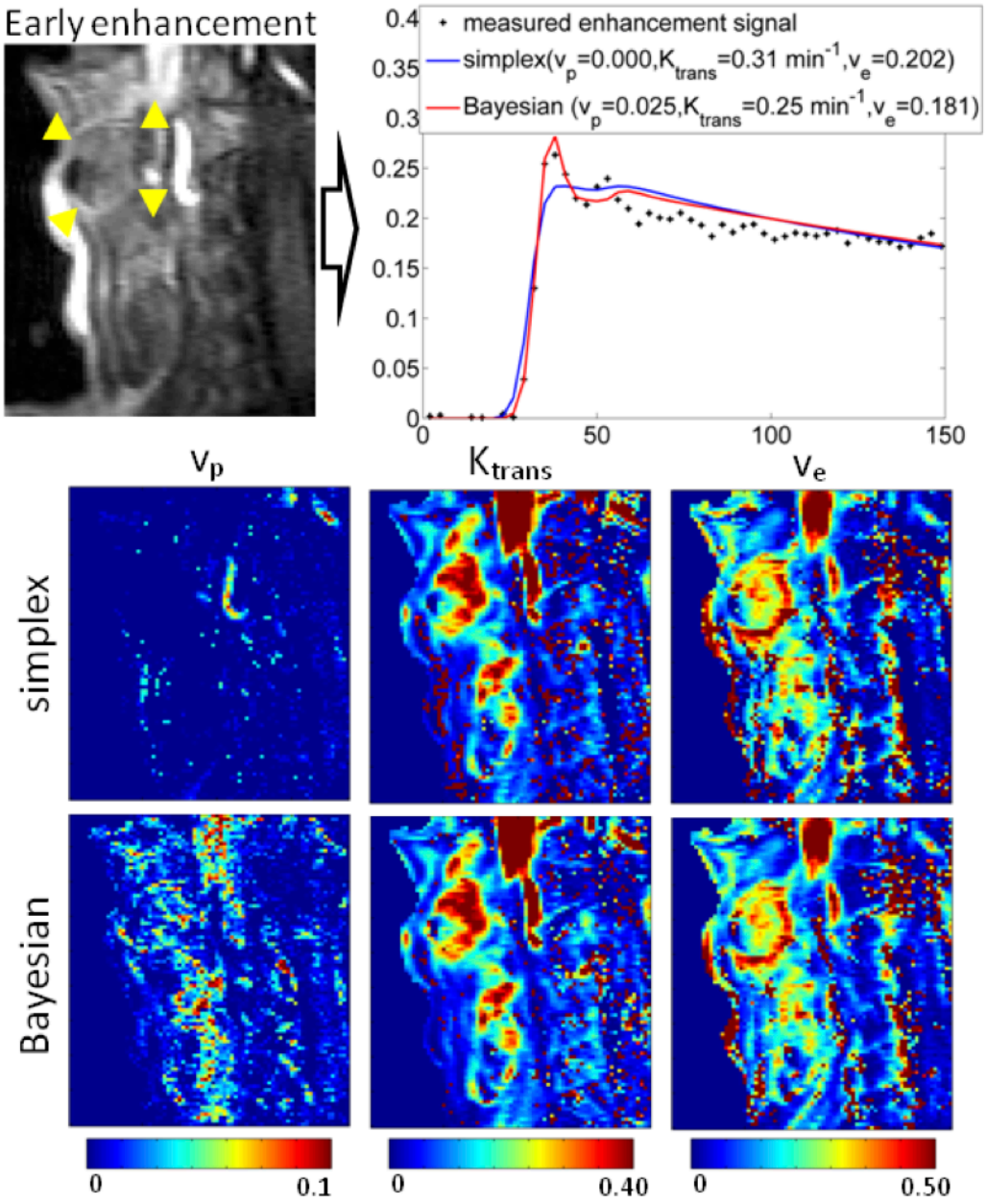

Figure 7. Box-plot diagram of the PK parameters derived with the simplex and the proposed Bayesian inference algorithms, performed separately for the benign and metastatic neck node ROIs. Asterisk (*) denotes significant difference ($p<0.05$) between the simplex and Bayesian inference algorithm.

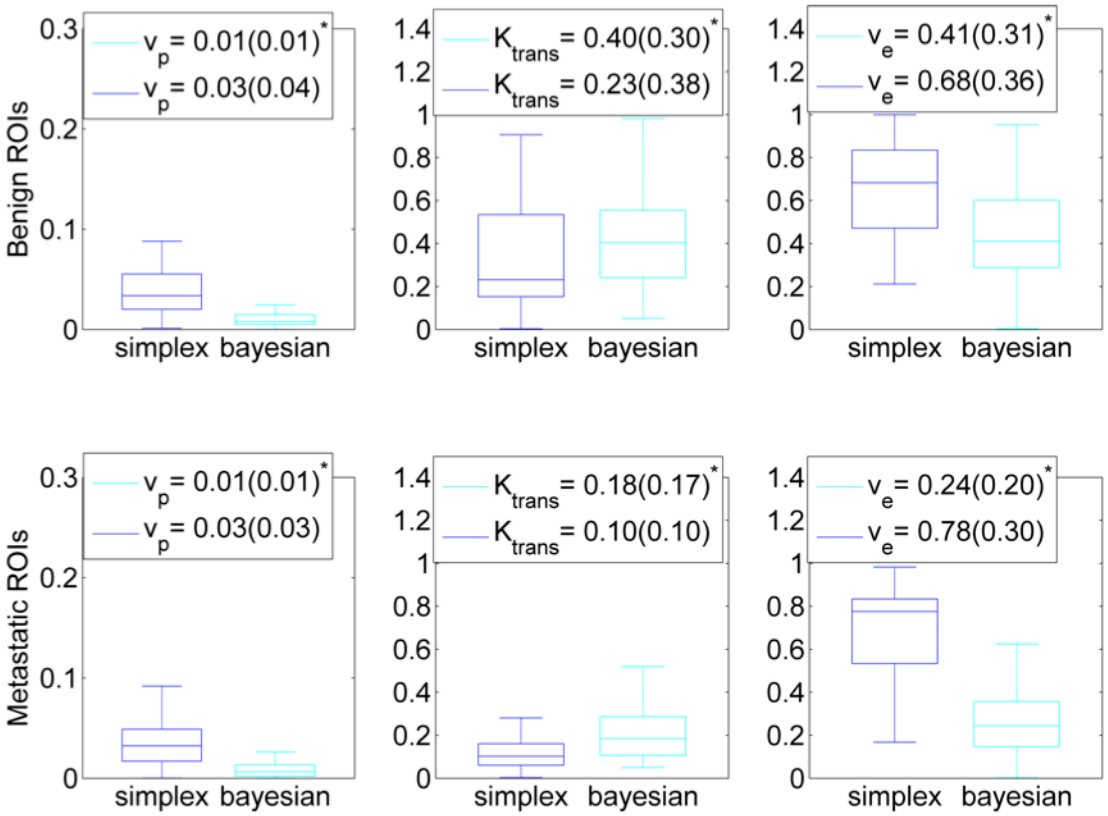

Figure 8. Example of nodal histograms on 100% oxygen compared with room air on a metastatic and normal nodes respectively.